First-principles calculations on effects of Al and Ga dopants on atomic and electronic structures of amorphous Ge$_2$Sb$_2$Te$_5$

Dongheon Lee (iD), Gijae Kang, Kyeongpung Lee, Sungjoon Yoon, Jeenu Kim, and Seungwu Han

View Online   Export Citation   CrossMark

First-principles calculations on effects of Al and Ga dopants on atomic and electronic structures of amorphous $Ge_2Sb_2Te_5$

View Online   Export Citation   CrossMark

Dongheon Lee,[1,a)] (iD) Gijae Kang,[1,a)] Kyeongpung Lee,[1] Sungjoon Yoon,[2] Jeenu Kim,[2] and Seungwu Han[1,b)]

AFFILIATIONS

[1]Department of Materials Science and Engineering and Research Institute of Advanced Materials, Seoul National University, Seoul 08826, South Korea

[2]R&D Division, SK Hynix Inc., 2091, Gyeongchung-daero, Babul-eup, Icheon-si, Gyeonggi-do 17336, South Korea

[a)]D. Lee and G. Kang contributed equally to this work.
[b)]Author to whom correspondence should be addressed: hansw@snu.ac.kr

ABSTRACT

Effects of post-transition metal dopants M (M = Al, Zn, and Ga) on structural and electronic properties of amorphous $Ge_2Sb_2Te_5$ (a-GST) are investigated through first-principles calculations based on the density functional theory. The doped a-GST is generated through the melt-quench procedure using molecular dynamics simulations. It is found that the three dopants behave similarly in a-GST, and they are mostly coordinated by Te atoms in tetrahedral geometry, which is similar to those in crystalline M_xTe_y. This is in contrast with crystalline GST wherein the most stable position of dopant M is the octahedral vacancy site. The number of wrong bonds such as Ge–Ge, Ge–Sb, or Sb–Sb increases as dopant atoms predominantly bond with Te atoms. The number of 4-fold ring structures, especially ABAB-type, decreases significantly, explaining the enhanced thermal stability of doped a-GST in the experiment. The bandgap estimated from density of states and the optical gap obtained from Tauc plot increase upon doping, which is also in good agreement with the experiment. By successfully relating the experimental doping effects and changes in the atomic structure, we believe that the present work can serve as a key to offer better retention and lower power consumption in phase-change memory.

I. INTRODUCTION

Phase-change memory (PCM) is a promising candidate for the next-generation nonvolatile memory owing to its advantages such as scalable high-density data storage,[1] low power consumption,[2] and long-term memory retention.[3] The working principle of PCM is based on contrasting electrical resistances between crystalline and amorphous phases that are rapidly and reversibly switchable using voltage pulses.[4,5] Recently, the PCM is attracting renewed interests as it enables a new stackable memory type (so called 3D XPoint memory) that combines the merits of the dynamic-random-access memory and the flash memory.[6] For the phase-changing materials, pseudobinary chalcogenides along the GeTe-Sb_2Te_3 tie line, in particular, $Ge_2Sb_2Te_5$ (GST) is most favored owing to fast crystallization speed and stability of amorphous phases.[7]

In spite of the notable device performance of GST-based PCM, further improvements are needed in specifications like data retention, power consumption, and switching speed to compete with the current memory type on the market. At the material level, this can be achieved by tuning relevant properties of chalcogenides. For instance, the retention (the speed) can be improved by increasing (decreasing) the crystallization temperature while higher electrical resistances in the crystalline phase can reduce power consumption by efficiently delivering the heating energy.

One popular approach to tuning the material property is external doping. So far, a wide range of dopants like C,[8–14]

N,[15–22] O,[17,18,22,23] Al,[24–26] Si,[22,27–29] Sc,[30] Ti,[30] V,[30,31] Cr,[30–34] Mn,[30,31,34–37] Fe,[30,31,38,39] Co,[30,34] Ni,[30,34] Cu,[30] Zn,[30,37,40,41] Ga,[42] Ag,[43–46] In,[47,48] Sn,[48–50] and Bi[48,50–52] were investigated for optimizing the material property of chalcogenides for the application to PCM. These dopants can be broadly classified according to their chemical natures: p-block elements (C, N, O, and Si), transition metals (Sc, Ti, V, Cr, Mn, Fe, Co, Ni, and Cu), and post-transition metals (Al, Zn, Ga, Ag, In, Sn, and Bi). A multitude of experiments confirmed that p-block elements such as C, N, O, and Si stabilize amorphous GST (a-GST) by increasing the crystallization temperature and activation barrier against crystallization.[8–11,15–18,27–29] In addition, they suppress the grain growth, reducing the grain size during crystallization. These dopants also reduce the reset (amorphization) current by increasing the electrical resistance in the crystalline state, which may originate from an increase in the structural disorder and optical gap.[8,10,15–17,27,28] However, phase separations were observed in N-, O-, and Si-doped GST, degrading the endurance property.[17–20] On the other hand, 3d transition metal dopants were investigated mainly for application to spintronics. The PCM with these dopants displayed distinct magnetic properties between crystalline and amorphous states, which has the potential for the multi-level memory.[32,33,35,36,38] The transition metal dopants also improved the thermal stability of the amorphous phase. Finally, for the post-transition metal dopants, it was found that Al, Zn, and Ga dopants improved the thermal stability of the amorphous phase and increased the bandgap,[24,25,40–42] which is similar to the effects of p-block elements. In contrast, In, Sn, Ag, and Bi doping led to low crystallization temperature and rapid crystallization.[47–51]

The doped chalcogenides have also been studied theoretically using the density functional theory (DFT) calculations, revealing the microscopic origin of property tuning by dopants. The p-block dopants increased the covalent character of Ge atoms, disrupting cubic or planar structures, which effectively suppress the crystallization process.[12–14,21,22] The transition metals were found to form various configurations from tetrahedral to octahedral, and stable magnetic states were obtained with V, Cr, Mn, and Fe.[30,31,34,37,39] Among the post-transition metal elements, Zn, Ag, and Bi were theoretically studied. Zn was found to undergo a large structural shift from tetrahedral to octahedral coordination upon crystallization[37] while Ag doping lead to faster phase transition and reduced the optical gap,[46] consistent with the experiment. Bi was found to substitute Sb and enhanced the crystallization speed by stabilizing planar structures like 4-fold rings.[52]

Among the previous calculations, less attention was paid to the small-size post-transition metal dopants such as Al and Ga although they were capable of tuning the material property of GST.[24–26,42] Motivated by this, herein, we theoretically investigate these dopants using DFT calculations. In particular, we focus on revealing impacts of these dopants on the structural and electronic properties in the amorphous phase and try to relate them to the experimental observations. For the comparison purpose, we also consider the Zn dopant because of its chemical similarity to Al and Ga. Doped amorphous GST models are generated with melt-quench simulations using DFT molecular dynamics (MD). We find that the three dopants show similar behaviors as they are mostly surrounded by four Te atoms in a tetrahedral geometry. Since dopants bond with significant numbers of Te atoms, the homopolar bonds among Ge or Sb increase in the doped systems, which enhance electron localization near the mobility edge. Furthermore, we find that these dopants increase the mobility gap and optical gap, which is in good agreement with the experiment.

II. COMPUTATIONAL METHODS

In order to generate Al-, Zn-, and Ga-doped a-GST, we carry out DFT MD simulations using the Vienna *Ab initio* Simulation Package (VASP).[53] The exchange-correlation energy among electrons is described by the generalized-gradient approximation.[54] The pseudopotential with the projector-augmented-wave type[55] is employed with the choice of valence subshells as $4s^24p^2$ (Ge), $5s^25p^3$ (Sb), $5s^25p^4$ (Te), $3s^23p^1$ (Al), $4s^24p^1$ (Ga), and $3d^{10}4s^2$ (Zn). The energy cutoff for the plane-wave basis is chosen to be 200 eV for MD and 400 eV for the structural relaxation. A single (0.25, 0.25, 0.25) point is sampled for the Brillouin-zone integration during MD while the cell geometry and atom position are optimized with $2 \times 2 \times 2$ Monkhorst-Pack grid. Since the DFT calculation underestimates the bandgap significantly, we additionally carry out the hybrid-functional (HSE06) calculations to obtain reliable bandgaps.[56–58] In the HSE06 calculation, the density of states (DOS) is computed with k points sampled on the $2 \times 2 \times 2$ grid, and the structures optimized in the PBE functional are used.

The amorphous structures are generated following the conventional melt-quench simulation.[59] Initially, 144 atoms of GST with 16 or 36 metal atoms (the corresponding doping concentration is 10 at. % and 20 at. %, respectively) are randomly put into a cubic box. The lattice parameters are set to match the mass density of GST to the theoretical value of undoped amorphous GST (5.6 g/cm³ or 0.0296 atoms/Å³), which is similar to the experimental value of 0.0309 atoms/Å³.[60,61] The volume expansion upon doping is considered by using the same mass density both for undoped and doped structures. In choosing the composition, we considered that the composition of GST was maintained to be 2:2:5 in the Al-doped GST.[24] The structures are pre-melted at 2000 K for 10 ps and melted at 1000 K for 30 ps to reach thermal equilibrium. The liquid is then quenched to 300 K with the quenching rate of –15 K/ps. The time step for the MD process is set to 2 fs. Finally, the amorphous structures are obtained by fully relaxing the structure including cell shape and volume. The resulting equilibrium densities are 0.029, 0.030, 0.029, and 0.029 atoms/Å³ for undoped, Al-, Zn-, and Ga-doped GST, respectively. The volume change from the starting value is less than 5%. Five amorphous structures are independently generated for each species of the metal dopant. We also additionally generate two Al-doped structures with 320 atoms to check cell-size effects, and it is found that the results from

the bigger cells are equivalent to those with 144 atoms (see Fig. S1 in the supplementary material). For the comparison purpose, undoped amorphous GST is also generated following the same procedure.

The bandgap of amorphous materials is defined as the energy difference between mobility edges in the valence and conduction bands, which separate localized states from extended states.[63] The bandgap dictates the resistivity of amorphous materials because electrical conduction occurs by thermally activating carriers trapped at the localized state above the mobility edge. In order to investigate the influence of dopants on the bandgap, we estimate the bandgap of amorphous GST in two independent ways as illustrated in Fig. 1 for undoped a-GST. First, we average DOS of amorphous models by aligning them with respect to the Te core level [see Fig. 1(a)]. (For metal-doped GST, Te atoms that are not bonded to the dopant are considered.) In order to determine mobility edges, the averaged DOS is fitted with the square root function form, $DOS \propto \sqrt{|E - E_{v(c)}|}$. The fitting ranges [shaded region in Fig. 1(a)] are chosen to give the best goodness of fit. The bandgap then corresponds to $E_c - E_v$. In undoped a-GST in Fig. 1(a), we obtain 0.39 eV for the bandgap. We also carry out similar fitting with DOS obtained by the hybrid functional (see above), which results in 0.72 eV. This is in excellent agreement with the experimental result of 0.7 eV.[24,41,62]
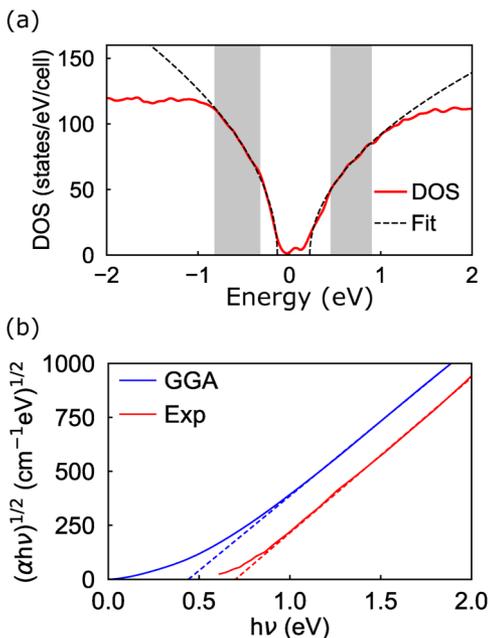
Second, we calculate the optical gap from the Tauc plot as shown in Fig. 1(b). The absorption coefficient α is calculated by the linear response theory based on the computed band structures.[64] The absorption coefficient of amorphous semiconductors generally follows a relationship of the form

$$\alpha h\nu = (\text{constant})(h\nu - E_{\text{opt}})^2, \qquad (1)$$

where h is the Planck constant, ν is the photon frequency, and E_{opt} is the optical bandgap. Equation (1) assumes a parabolic band for the amorphous semiconductors.[65] The optical gap is determined by linearly extrapolating the plot of $(\alpha h\nu)^{1/2}$ vs $h\nu$ (so called the Tauc plot) and finding the intercept with the abscissa. Figure 1(b) compares the theoretical and experimental Tauc plot, showing that the two curves are similar except for the rigid shift. The estimated optical gap is 0.43 eV, in reasonable agreement with the bandgap of 0.39 eV estimated from the mobility edges in DOS (see above).

III. RESULTS AND DISCUSSIONS

We first identify stable dopant sites in the crystalline GST (c-GST). As candidate sites, we consider vacancy site (octahedral configuration), interstitial site (cube center), Ge, Sb, or Te substitutional sites. Due to the random occupation of cations in c-GST, three different sites for each type of defects are examined and only those with the lowest energies are considered. By comparing the defect formation energy, we find that the octahedral vacancy sites are the most preferable sites in the c-GST for every dopant.

Next, we discuss the influence of dopants on the structure of a-GST. Here the discussion is mainly based on the result with 10 at. % doping. The result from higher doping concentration (20 at. %) for Al and Zn which is consistent with 10 at. % doping is presented in the supplementary material. Figure 2(a) compares radial distribution functions (RDFs) of undoped and doped a-GST. It is seen that RDFs for doped a-GST are similar regardless of the dopant element. While the medium-range order beyond ~4 Å does not change meaningfully with doping, the positions of the first peak are shortened in doped a-GST. As will be discussed in the below, this is due to the relatively short metal–Te (M–Te) bonds.

Figures 2(b)–2(d) show the representative atomic structures of Al-, Zn-, and Ga-doped a-GST, respectively. For visual clarity, dopants and neighboring atoms are highlighted in the ball-and-stick style while other atoms are represented by wireframes. It is noticeable that dopants predominantly bond with Te atoms. Such metal-chalcogen bonds are stabilized by the large difference in electronegativity. The detailed environment around each dopant can be quantified by the atom-resolved coordination number (CN) as shown in Fig. 3(a). It is intriguing that the CN for every dopant is around four (hatched rectangle), which hints tetrahedral coordinations. This is confirmed by the bond-angle distributions (not shown) around dopants that peak at 109°. These structural units are similar to those in the crystalline Al_2Te_3 ($P2_1/c$), ZnTe ($F\bar{4}3m$), and Ga_2Te_3 (Cc), where metal atoms are also tetrahedrally coordinated with four Te atoms. This is also consistent with

FIG. 1. (a) The density of states (DOS) and (b) Tauc plot of undoped a-GST. The shaded areas are the energy region used for fitting DOS to square root forms (dashed lines). Experimental data in (b) Tauc plot is obtained from Ref. 62.
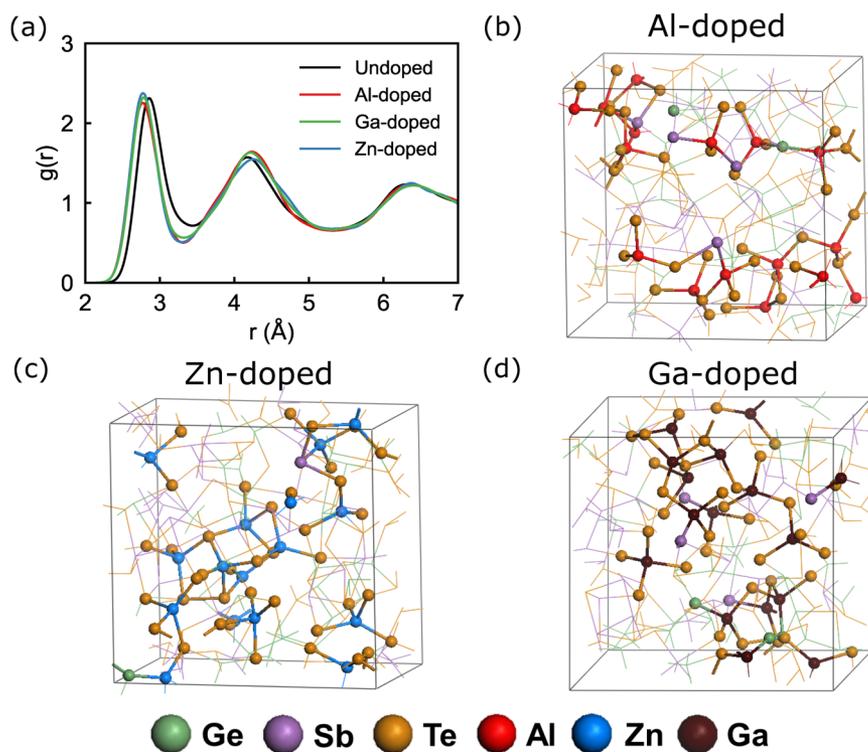
FIG. 2. (a) Radial distribution functions of undoped and doped a-GST and amorphous structure of (b) Al-, (c) Zn-, and (d) Ga-doped a-GST. Only atoms coordinated with dopants are drawn in ball-and-stick models.

the previous work on Zn dopants in a-GST.[30,37] It is interesting that the similar local environment is observed in alloy systems with different chalcogenide systems, such as AlSbTe or GaSbTe alloy[68,69] in which both Al and Ga atoms prefer to bond with Te atoms forming tetrahedral configuration. In Fig. 3(a), it is seen that Ga dopants bond with Ge and Sb atoms slightly more than Al or Zn dopant. This is because electronegativity of Ga (1.81) is larger than for Al (1.61) and Zn (1.65), and so less ionic Ga can bond with Ge or Sb more strongly than Al or Zn. The average M–Te lengths in Al-, Zn-, and Ga-doped a-GST estimated by the first-peak position in the pair distribution function (not shown) are 2.66, 2.68, and 2.69 Å, respectively (see Table I). The present Zn–Te and Ga–Te bond lengths are very close to that in 1% Zn-doped GST, 2.67 Å and that in Ga–Sb–Te alloy, 2.70 Å.[30,69] These are shorter than Ge–Te or Sb–Te lengths in Table I, which results in the shorter first peak in doped a-GST in Fig. 2(a).

In order to understand how dopants affect bonding network in a-GST, we analyze atom-resolved CN for doped GST in Figs. 3(b)–3(d). It is seen that every atom type maintains similar total CNs regardless of doping. Since dopants mainly bond with Te, partial CNs of Te with Ge and Sb decrease. This in turn increases homopolar bonds such as Ge–Ge, Ge–Sb, and Sb–Sb as can be confirmed in Figs. 3(b) and 3(c). The average number of such homopolar bonds increases from 18.6 in

undoped GST to 38.8 (Al-doped), 30.6 (Zn-doped), and 28.2 (Ga-doped). In contrast, anionic Te–Te homopolar bonds decreased in number [see Fig. 3(d)] because of strong M–Te bonds. We also find that dopant–dopant bonds are hardly formed due to the strong cationic character of the dopant (only one Ga–Ga bond is found in all samples).

The average Bader charge for each element is compiled in Table II. Atoms that are bonded to the metal dopants have more negative charges compared to those in undoped a-GST, which confirms that the dopants in a-GST take on the cationic character. The charges of dopants are almost the same as in the crystalline phase of Al_2Te_3, $ZnTe$, and Ga_2Te_3, implying that M–Te bonds are similar to those in the compound phase. We also note that the charges of the atoms that are not directly bonded are similar with those in undoped GST.

In experiments, Al, Zn, and Ga dopants were found to stabilize the amorphous phase by increasing the crystallization temperature.[24,25,40–42] In a-GST, the stability of the amorphous phase has been indirectly assessed by the distribution of the ring structure. The decrease (increase) of ABAB-type (A = Ge or Sb, B = Te) 4-fold rings tends to stabilize (destabilize) the amorphous phase because they resemble crystalline building blocks and serve as nucleation sites.[12,66] Therefore, we analyze the population of the ring structure shown in Fig. 4. Since the number of atoms in doped GST is larger than
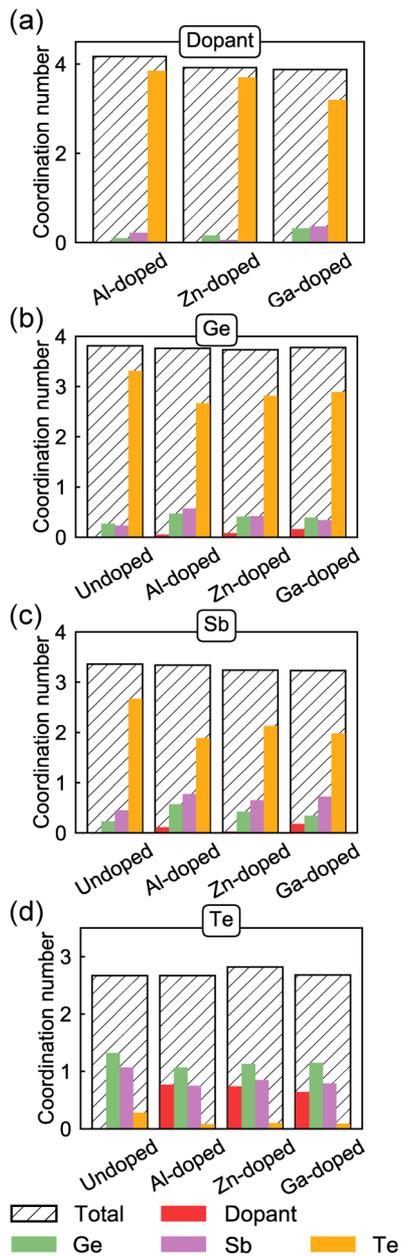
FIG. 3. Average coordination numbers around (a) dopant (b) Ge, (c) Sb, and (d) Te, which is calculated from the pair distribution functions of undoped and doped a-GST. For all pairs, the cutoff radius was set to be 3.2 Å. The hatched rectangles represent the total coordination numbers.

TABLE I. Average bond lengths of atoms in undoped and doped a-GST (all values are in Å).

	Undoped	Al-doped	Zn-doped	Ga-doped
M−Te		2.66	2.68	2.69
Ge−Te	2.79	2.78	2.77	2.78
Sb−Te	2.92	2.93	2.91	2.91

Fig. 3). Since crystallization from odd-numbered ring requires the breaking of several bonds,[66] the increased number of homopolar bonds in doped a-GST indicates that the stability of the amorphous phase is enhanced. In the inset of Fig. 4, we present the number of ABAB-type 4-fold rings, and it is shown that every doped GST has less ABAB-type rings than undoped GST. This also indicates higher stability of the amorphous phase. The enhanced stability inferred from the ring structures is consistent with the increase of the crystallization temperature in the experiment. (The direct estimation of the crystallization temperature using *ab initio* simulation is not feasible since the crystallization of GST requires simulation time at least several nanoseconds.)

Since the crystallization temperature and crystallization speed often shows trade-off relationship,[70] the metal doping may imply slower crystallization kinetics. Indeed, it was reported that the crystallization activation energy for other chalcogenide increased upon Al doping.[71] However, it seems that inconsistencies exist among the experimental data on the crystallization kinetics. For example, Ref. 26 reported faster crystallization for the Al-doped GST, but the measured crystallization temperature was at variance with other experimental works.[24,25] Reference 42 investigated the effect of Ga doping on the activation energy, but the composition of the GST changed upon doping and the activation energies did not show coherent tendency with respect to the doping concentration. Thus, while the amorphous stability was consistently enhanced with doping, the influence on crystallization kinetics needs further experimental investigation.

Theoretically, some of the recent works reported the *ab initio* simulation of crystallization kinetics for a-GST.[46,52] To address the crystallization kinetics of doped a-GST in a similar way, we perform crystallization simulations for 500 ps at 600 K with undoped a-GST and Al-doped a-GST. However,

for undoped GST (160 versus 144), the total counts of ring structures increase accordingly. Nevertheless, it is noticeable that 5-fold and 7-fold ring structures significantly increase in every doped a-GST. This is because the doping promotes homopolar bonds such as Ge–Ge, Ge–Sb, and Sb–Sb (see

TABLE II. Average atomic charges in the undoped and Al-, Zn-, and Ga-doped a-GST. "bo" represents atoms bonded to dopants, and "nb" are other atoms. The values in parenthesis are atomic charges in the crystalline phase. All values are given in (positive) electronic charge.

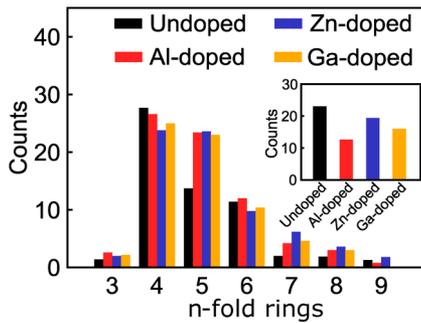|	Undoped	Al-doped		Zn-doped		Ga-doped	
		bo	nb	bo	nb	bo	nb
Ge	0.35	−0.14	0.31	0.27	0.32	0.16	0.33
Sb	0.41	−0.18	0.32	0.12	0.34	0.17	0.33
Te	−0.30	−0.72	−0.33	−0.37	−0.31	−0.36	−0.32
Dopant		1.73 (1.80)		0.47 (0.57)		0.49 (0.53)	

FIG. 4. Ring statistics for undoped and doped *a*-GST counted per supercell. The number of ABAB-type 4-fold rings is shown in the inset (A = Ge or Sb, B = Te).
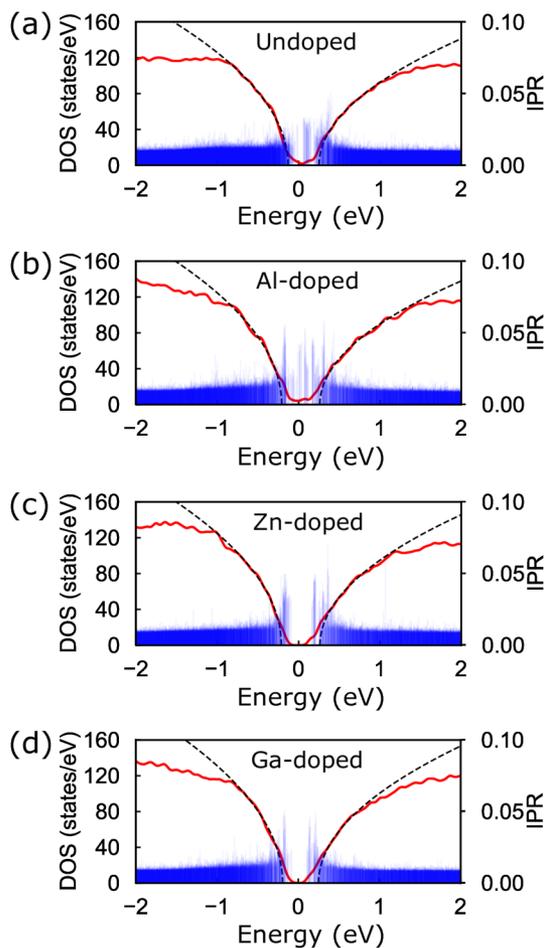
TABLE III. Calculated bandgap and optical gap of undoped and doped *a*-GST. The optical gap measured in experiments is also listed. The values in parenthesis are calculated using HSE06 functional. All values are in eV.

	Bandgap	Optical gap	Exp.
Undoped	0.39 (0.72)	0.43	0.70,[a,b] 0.90[c]
Al-doped	0.47 (0.84)	0.49	0.76[a]
Zn-doped	0.47 (0.86)	0.50	0.78,[b] 1.10[c]
Ga-doped	0.44 (0.80)	0.48	...

[a]Reference 24.
[b]Reference 41.
[c]Reference 40.

we could not observe the crystallization within the given simulation time. We note that the onset time for the crystallization vary over a few hundred picoseconds and is affected by initial amorphous structures.[46]

In Fig. 5, DOSs for undoped and doped *a*-GST are presented. The mobility edge can be identified by fitting DOS to the square root function (see Sec. II) as indicated by the dashed lines. The resulting bandgaps are shown in Table III and compared with the experimental data. The bandgap in the parenthesis is calculated using the HSE06 functional. The differences between the bandgap and optical gap in DFT are within 0.04 eV, supporting consistency between the two methods to estimate the energy gap in *a*-GST. In the experiment, the optical gap of *a*-GST was measured to be 0.70 eV[24,41,62] while that of doped GST with 14 at. % of Al dopants was 0.76 eV.[24] Doping of 15 at. % Zn also increased the optical gap to 0.78 eV.[41] These results are consistent with the present results wherein the bandgaps of undoped, Al-doped, and Zn-doped GST are 0.72, 0.84, and 0.86 eV, respectively. The doping of Ga in GST with 2:2:5 composition has not been reported yet but 13 at. % doping of Ga into $Ge_3Sb_2Te_5$ decreased the optical gap from 0.75 eV to 0.71 eV,[42] which appears to contradict the present computational result. However, we note that in Ref. 42, the composition of $Ge_3Sb_2Te_5$ was changed to 24:29:34 after the Ga doping. The reduced bandgap in the experiment might be a result of this compositional change, especially the reduction in Te density.

In the experiment, the bandgap of Al-doped GST increased linearly with the doping concentration. In order to reproduce this, bandgap energies of undoped, 10 at. %, and 20 at. % of Al- and Zn-doped *a*-GST are compared with the measured bandgap of Al-doped GST.[24] It is found that the bandgap increases almost linearly with doping density up to 20 at. %. The slopes of the linearly fitted lines for Al and Zn doping are 0.0053 and 0.0051 eV/at. %, respectively, and the slope for experimental data is 0.0042 eV/at. % for Al doping (see Fig. S2 in the supplementary material). Therefore, the trend of bandgap increase upon metal doping is well reproduced in the calculation. This bandgap widening is attributed to changes in local compositions around host atoms. Most of the metal dopants are surrounded by Te atoms and exist as MTe_4 units. These local structures and chemical environments are similar to those in crystalline phase M_xTe_y, and

FIG. 5. DOS (solid curves) and IPR (vertical lines) of (a) undoped, (b) Al-, (c) Zn-, and (d) Ga-doped GST. The energies are referenced to the Fermi level of each system. The dashed lines are the square root functions fitted to DOS.

so metal-doped a-GST can be regarded as mixtures of GST and M_xTe_y. The bandgaps calculated by the present HSE06 calculations are 1.90, 2.05, and 1.83 eV for Al_2Te_3, ZnTe, and Ga_2Te_3, respectively, rationalizing the bandgap increase in the mixture phase.[67] As the metal doping concentration increases from 10 at. % to 20 at. %, the number density of $AlTe_4$ ($ZnTe_4$) units increases from $1.7/nm^3$ ($1.9/nm^3$) to $2.6/nm^3$ ($3.0/nm^3$), which in turn widens the bandgap of doped a-GST.

We also calculate the dielectric function of the a-GST to compare the optical properties of doped and undoped a-GST (see Fig. S4 in the supplementary material). In low photon energy (below 0.5 eV), the calculated refractive index (n) of undoped a-GST is 5.4 and those of doped a-GST is 4.9, 4.7, and 4.9 for Al, Zn, and Ga, respectively. (The experimental values for undoped a-GST range from 3.3 to 4.5.[72,73]) The changes in the calculated extinction coefficients (k) by Al doping are qualitatively matched to results from the experiment in which the doping lowers the k of a-GST.[25] The refractive index and extinction coefficient decrease with metal doping, which is originated from the bandgap increase of doped a-GST.

In order to examine the degree of localization for states near the mobility edges, we present in Fig. 5 the inverse participation ratio (IPR) that is defined as follows:

$$IPR = \frac{\sum_1^N w_i^2}{\left(\sum_1^N w_i\right)^2}, \qquad (2)$$

where N is the total number of atoms in the supercell and w_i is the partial weight of the given state on the ith atom. If the state is evenly distributed over entire atoms, IPR becomes $1/N$, while it approaches one when it is localized over a few atomic sites. In Fig. 5, compared to IPR of undoped GST, those of metal-doped GSTs show higher values near the mobility edges. We find that the localized states near the conduction mobility edge are typically concentrated at the wrong bonds like Ge–Ge, Ge–Sb, or Sb–Sb. On the other hand, states near the valence mobility edge are mainly lone pairs at Te atoms. Both bandgap increase and stronger localization near the mobility edge imply that the electrical resistance of doped a-GST is likely to be higher than for undoped a-GST. Indeed, the R-T curves measured for Al-,[24,26] Zn-,[40,41] and Ga-doped[42] a-GST equally show the increase of the electrical resistance in the doped a-GST.

IV. CONCLUSIONS

In conclusion, we generated Al-, Zn-, and Ga-doped a-GST using first-principles calculations and analyzed the effects of dopants on atomic and electronic properties. While the local geometry of host atoms shows only subtle changes upon doping, the detailed information such as ring statistics and coordination number indicates that the doping induces wrong bonds like Ge–Ge, Ge–Sb, and Sb–Sb, which can hinder the crystallization of a-GST and result in the higher stability of the amorphous phase. The metal dopants in a-GST mostly bond to Te atoms having 4-fold coordination, which

resembles MTe_4 units in crystalline M_xTe_y and explains the bigger bandgap of doped a-GST. The calculated bandgaps for undoped, Al-, Zn-, and Ga-doped a-GST are 0.72, 0.84, 0.86, and 0.80 eV, respectively, which show good agreement with extant experimental measurements. We believe that the present work suggests a promising doping strategy for higher stability and a wider bandgap, which in turn serve as a key to offer better retention and lower power consumption in the PCM.

SUPPLEMENTARY MATERIAL

See supplemental material for the structural and electronic properties of doped a-GST with different doping densities and larger cell size, and the calculated refractive index.

REFERENCES

[1]S. Raoux, G. W. Burr, M. J. Breitwisch, C. T. Rettner, Y. C. Chen, R. M. Shelby, M. Salinga, D. Krebs, S. H. Chen, H. L. Lung, and C. H. Lam, J. Res. Dev. **52**, 465 (2008).
[2]F. Xiong, A. D. Liao, D. Estrada, and E. Pop, Science **332**, 568 (2011).
[3]S. Song, Z. Song, L. Wu, B. Liu, and S. Feng, J. Appl. Phys. **109**, 034503 (2011).
[4]N. Yamada, E. Ohno, K. Nishiuchim, and N. Akahira, J. Appl. Phys. **69**, 2849 (1991).
[5]W. J. Wang, L. P. Shi, R. Zhao, K. G. Lim, H. K. Lee, T. C. Chong, and Y. H. Wu, Appl. Phys. Lett. **93**, 043121 (2008).
[6]J. Choe, in Flash Memory Summit 2017 Proceedings, Santa Clara, CA, 7–10 August 2017.
[7]L. Wang, C.-H. Yang, and J. Wen, Electron. Mater. Lett. **11**, 505 (2015).
[8]X. Zhou, L. Wu, Z. Song, F. Rao, M. Zhu, C. Peng, D. Yao, S. Song, B. Liu, and S. Feng, Appl. Phys. Lett. **101**, 142105 (2012).
[9]Q. Hubert, C. Jahan, V. Sousa, L. Perniola, A. Kusiak, J.-L. Battaglia, P. Noé, M. Bernard, C. Sabbione, M. Tessaire, F. Pierre, P. Zuliani, R. Annunziata, G. Pananakakis, and B. de Salvo, in 2013 International Conference on Solid State Devices and Materials, Fukuoka, 24–27 September 2013.
[10]J. H. Park, S.-W. Kim, J. H. Kim, Z. Wu, S. L. Cho, D. Ahn, D. H. Ahn, J. M. Lee, S. U. Nam, and D.-H. Ko, J. Appl. Phys. **117**, 115703 (2015).
[11]W. Zhou, L. Wu, X. Zhou, F. Rao, Z. Song, D. Yao, W. Yin, S. Song, B. Liu, B. Qian, and S. Feng, Appl. Phys. Lett. **105**, 243113 (2014).
[12]E. Cho, Y. Youn, and S. Han, Appl. Phys. Lett. **99**, 183501 (2011).
[13]X. Zhou, M. Xia, F. Rao, L. Wu, X. Li, Z. Song, S. Feng, and H. Sun, ACS Appl. Mater. Interfaces **6**, 14207 (2014).
[14]K. B. Borisenko, Y. Chen, D. J. H. Cockayne, S. A. Song, and H. S. Jeong, Acta Mater. **59**, 4335 (2011).
[15]Y. Kim, K. Jeong, M.-H. Cho, U. Hwang, H. S. Jeong, and K. Kim, Appl. Phys. Lett. **90**, 171920 (2007).
[16]K.-H. Song, J.-H. Kim, J.-H. Seo, and H.-Y. Lee, J. Optoelectron. Adv. M. **11**, 1988 (2009).
[17]S. Privitera, E. Rimini, and R. Zonca, Appl. Phys. Lett. **85**, 3044 (2004).
[18]S. Privitera, E. Rimini, C. Bongiorno, A. Pirovano, and R. Bez, Nucl. Instrum. Methods Phys. Res. B **257**, 352 (2007).

[19]K. Kim, J.-C. Park, J.-G. Chung, S. A. Song, M.-C. Jung, Y. M. Lee, H.-J. Shin, B. Kuh, Y. Ha, and J.-S. Noh, Appl. Phys. Lett. **89**, 243520 (2006).

[20]M.-C. Jung, Y. M. Lee, H.-D. Kim, M. G. Kim, H. J. Shin, K. H. Kim, S. A. Song, H. S. Jeong, C. H. Ko, and M. Han, Appl. Phys. Lett. **91**, 083514 (2007).

[21]T. H. Lee, D. Loke, and S. R. Elliott, Adv. Mater. **27**, 5477 (2015).

[22]E. Cho, S. Han, D. Kim, H. Horii, and H.-S. Nam, J. Appl. Phys. **109**, 043705 (2011).

[23]M. H. Jang, S. J. Park, D. H. Lim, M.-H. Cho, K. H. Do, D.-H. Ko, and H. C. Sohn, Appl. Phys. Lett. **95**, 012102 (2009).

[24]G. Wang, X. Shen, Q. Nie, R. Wang, L. Wu, Y. Lv, F. Chen, S. Dai, and J. Li, J. Phys. D Appl. Phys. **45**, 375302 (2012).

[25]S. Wei, J. Li, X. Wu, P. Zhou, S. Wang, Y. Zheng, L. Chen, F. Gan, X. Zhang, and G. Li, Opt. Express **15**, 10584 (2007).

[26]J.-H. Seo, K.-H. Song, and H.-Y. Lee, J. Appl. Phys. **108**, 064515 (2010).

[27]Y. Ling, Y. Lin, B. Qiao, Y. Lai, J. Feng, T. Tang, B. Cai, and B. Chen, Jpn. J. Appl. Phys. **45**, L349 (2006).

[28]B. Qiao, J. Feng, Y. Lai, Y. Ling, Y. Lin, T. Tang, B. Cai, and B. Chen, Appl. Surf. Sci. **252**, 8404 (2006).

[29]J. Feng, Y. Zhang, B. W. Qiao, Y. F. Lai, Y. Y. Lin, B. C. Cai, T. A. Tang, and B. Chen, Appl. Phys. A **87**, 57 (2007).

[30]J. M. Skelton and S. R. Elliott, J. Phys. Condens. Matter **25**, 205801 (2013).

[31]T. Fukushima, H. Katayama-Yoshida, K. Sato, H. Fujii, E. Rabel, R. Zeller, P. H. Dederichs, W. Zhang, and R. Mazzarello, Phys. Rev. B **90**, 144417 (2014).

[32]Y. Fukuma, N. Nishimura, F. Odawara, H. Asada, and T. Koyanagi, J. Supercond. Incorporating Nov. Magn. **16**, 71 (2003).

[33]Q. Wang, B. Liu, Y. Xia, Y. Zheng, R. Huo, Q. Zhang, S. Song, Y. Cheng, Z. Song, and S. Feng, Appl. Phys. Lett. **107**, 222101 (2015).

[34]W. Zhang, I. Ronneberger, Y. Li, and R. Mazzarello, Adv. Mater. **24**, 4387 (2012).

[35]Y. Fukuma, H. Asada, M. Arifuku, and T. Koyanagi, Appl. Phys. Lett. **80**, 1013 (2002).

[36]H. Shingai, T. Kato, M. Kosuda, Y. Takagi, H. Oyake, and H. Hirata, Jpn. J. Appl. Phys. **49**, 08KG02 (2010).

[37]J. M. Skelton, T. H. Lee, and S. R. Elliott, Appl. Phys. Lett. **101**, 024106 (2012).

[38]W.-D. Song, L.-P. Shi, X.-S. Miao, and C.-T. Chong, Adv. Mater. **20**, 2394 (2008).

[39]Y. Li and R. Mazzarello, Adv. Mater. **24**, 1429 (2012).

[40]R. Li, Y. Jiang, L. Xu, Z. Ma, F. Yang, J. Xu, and W. Su, Phys. Status Solidi A **210**, 2650 (2013).

[41]G. Wang, Q. Nie, X. Shen, R. P. Wang, L. Wu, J. Fu, T. Xu, and S. Dai, Appl. Phys. Lett. **101**, 051906 (2012).

[42]Y. Lu, Z. Zhang, S. Song, X. Shen, G. Wang, L. Cheng, S. Dai, and Z. Song, Appl. Phys. Lett. **102**, 241907 (2013).

[43]D. H. Kim, M. S. Kim, R.-Y. Kim, K. S. Kim, and H. G. Kim, Mater. Charact. **58**, 479 (2007).

[44]K.-H. Song, S.-W. Kim, J.-H. Seo, and H.-Y. Lee, J. Appl. Phys. **104**, 103516 (2008).

[45]K.-H. Song, S.-W. Kim, J.-H. Seo, and H.-Y. Lee, Thin Solid Films **517**, 3958 (2009).

[46]B. Prasai, G. Chen, and D. A. Drabold, Appl. Phys. Lett. **102**, 041907 (2013).

[47]K. Wang, C. Steimer, D. Wamwangi, S. Ziegler, and M. Wuttig, Appl. Phys. A **80**, 1611 (2005).

[48]K. Wang, C. Steimer, D. Wamwangi, S. Ziegler, M. Wuttig, J. Tomforde, and W. Bensch, Microsyst. Technol. **13**, 203 (2007).

[49]W. D. Song, L. P. Shi, X. S. Miao, and T. C. Chong, Appl. Phys. Lett. **90**, 091904 (2007).

[50]T.-J. Park, S.-Y. Choi, and M.-J. Kang, Thin Solid Films **515**, 5049 (2007).

[51]K. Wang, D. Wamwangi, S. Ziegler, C. Steimer, and M. Wuttig, J. Appl. Phys. **96**, 5557 (2004).

[52]J. M. Skelton, A. R. Pallipurath, T.-H. Lee, and S. R. Elliott, Adv. Funct. Mater. **24**, 7291 (2014).

[53]G. Kresse and J. Hafner, Phys. Rev. B **47**, 558 (1993).

[54]J. P. Perdew, K. Burke, and M. Ernzerhof, Phys. Rev. Lett. **77**, 3865 (1996).

[55]P. E. Blöchl, Phys. Rev. B **50**, 17953 (1994).

[56]J. Heyd, G. E. Scuseria, and M. Ernzerhof, J. Chem. Phys. **118**, 8207 (2003).

[57]J. Heyd and G. E. Scuseria, J. Chem. Phys. **121**, 1187 (2004).

[58]S. Park, B. Lee, S. H. Jeon, and S. Han, Curr. Appl. Phys. **11**, S337 (2011).

[59]Y. Youn, Y. Kang, and S. Han, Comp. Mater. Sci. **95**, 256 (2014).

[60]E. Cho, J. Im, C. Park, W. J. Son, D. H. Kim, H. Horii, J. Ihm, and S. Han, J. Phys. Condes. Matter **22**, 205504 (2010).

[61]W. K. Njoroge, H.-W. Wöltgens, and M. Wuttig, J. Vac. Sci.Technol. A **20**, 230 (2002).

[62]B.-S. Lee, J. R. Abelson, S. G. Bishop, D.-H. Kang, B.-k. Cheong, and K.-B. Kim, J. Appl. Phys. **97**, 093509 (2005).

[63]R. Zallen, *The Physics of Amorphous Solids* (Wiley VCH, Weinheim, 2004).

[64]Y. Kang, H. Song, H.-H. Nahm, S. H. Jeon, Y. Cho, and S. Han, APL Mater. **2**, 032108 (2014).

[65]J. Tauc, R. Grigorovici, and A. Vancu, Phys. Status Solidi **15**, 627 (1966).

[66]K. Shinji, K. Kenichi, K. Shigeru, T. Hitoshi, U. Takeshi, S. Kentaro, T. Hiroshi, M. Yutaka, M. Toshiyuki, Y. Noboru, T. Yoshihito, S. Hiroyoshi, and T. Masaki, Appl. Phys. Lett. **89**, 201910 (2006).

[67]K. Yim, Y. Youn, J. Lee, K. Lee, H.-H. Nahm, J. Yoo, C. Lee, C. S. Hwang, and S. Han, NPG Asia Mater. **7**, e190 (2015).

[68]M. Xia, K. Ding, F. Rao, X. Li, L. Wu, and Z. Song, Sci. Rep. **5**, 8548 (2015).

[69]A. Bouzid, S. Garbardi, C. Massobrio, M. Boero, and M. Bernasconi, Phys. Rev. B **91**, 184201 (2015).

[70]S. Raoux and M. Wuttig, *Phase Change Materials: Science and Applications* (Springer, 2009), p. 389.

[71]C. Peng, L. Wu, Z. Song, F. Rao, M. Zhu, X. Li, B. Liu, L. Cheng, S. Feng, P. Yang, and J. Chu, Appl. Surf. Sci. **257**, 10667 (2011).

[72]W. H. P. Pernice and H. Bhaskaran, Appl. Phys. Lett. **101**, 171101 (2012).

[73]Z. Xu, C. Chen, Z. Wang, K. Wu, H. Chong, and H. Ye, RSC Adv. **8**, 21040 (2018).